Nanoscale Advances

PAPER

View Article Online
View Journal

Cite this: DOI: 10.1039/d6na00217j

Tuneable structural and environmental factors for stability of rosette nanotubes

Usha D. Hemraz, *[abc] Takeshi Yamazaki,[ab] Rachel L. Beingessner,[b] Jae-Young Cho[b] and Hicham Fenniri*[abd]

Rosette nanotubes (RNTs) are biocompatible tubular architectures self-assembled under physiological conditions from a self-complementary DNA base hybrid molecule which features the hydrogen-bonding arrays of both guanine and cytosine (G∧C motif). The formation of these architectures is a hierarchical process involving H-bonding and π–π stacking interactions. While motifs possessing either a single, twin or tetra G∧C bases form RNTs, twin RNTs are more versatile due to high stability stemming from intermolecular H bonding interactions, greater preorganization and amphiphilic character and ease of chemical modification. These twin RNTs experience a lower charge density and steric repulsion when functionalized on their outer surface. In order to fully exploit these organic materials which have an intrinsic stability suitable for biomedical and other materials applications, it was necessary to explore the factors that can optimize the self-assembly process and resulting RNT stability. Here we describe the synthesis and characterization of several single and twin G∧C modules that were used to produce self-assembled nanotubes and investigated key environmental and structural factors including solvent, counterions, outer RNT functionalization, G∧C core structure and charge on the self-assembly process.

Received 19th March 2026
Accepted 27th May 2026

DOI: 10.1039/d6na00217j

rsc.li/nanoscale-advances

Introduction

The self-assembly of simple monomeric building blocks into complex structures requires the coordination of both non-directional and directional non-covalent interactions.[1–7] Notable examples of natural self-assembled systems include the DNA double helix[2] and the coat protein of the tobacco mosaic virus.[8] These systems are remarkable due to their complexity and ability to form in physiological and aqueous environments, where competitive solvation of hydrogen donor and acceptor sites can influence intermolecular interactions. Less directional forces like hydrophobic contacts[9–11] and aromatic stacking interactions,[12] which are particularly strong in aqueous solutions, assist in achieving strong complexation. Using nature as inspiration, a myriad of artificial nanostructures self-assembled in water and protic solvents have emerged; some of which include capsules,[13–16] vesicles,[17–19] and wires.[20–23] While the properties and stability of these and other supramolecular architectures largely depend on the structure of the monomers themselves, the formation and strength of the non-covalent bonds can be mediated by their surrounding environment. This allows for both internal control (*e.g.* monomer structure) and external control (*e.g.*, pH, solvent, temperature) over the self-assembly process.

Rosette Nanotubes (RNTs) are formed through the self-assembly of a self-complementary heterobicyclic DNA base hybrid molecule that integrates the hydrogen-bonding patterns of both guanine and cytosine (G∧C motif).[24–27] The self-assembly process is hierarchical, beginning with the formation of hexameric rosettes stabilized by hydrogen bonding interactions, followed by π–π stacking of these supermacrocycles to form the RNTs. The versatility of these organic nanotubes, due to their ease of chemical modification and biocompatibility, have made them suitable candidates for various biomedical applications including tissue engineering materials and delivery applications.[28–37] We have developed the single,[24,25] twin[26,27] and quad[38] G∧C systems, all of which self-assemble by an initial rosette formation through 18, 36 and 72 intermolecular hydrogen bonding interactions per rosette, respectively. While the quad rosette system does offer enhanced stability due to the higher number of intermolecular hydrogen bonding interactions (72 *vs.* 36), the twin rosette system provides a wider scope for functional group diversification. We have designed twin RNTs with a wide range of attachments, including amino acids,[26,27] peptides,[30,33] a fluorescent group[34] and chiral groups.[27] We have also shown that the twin G∧C system can be functionalized with up to 15 lysine residues and the resulting modules formed nanotubes under aqueous conditions.[27]

[a]*Department of Chemistry, University of Alberta, 11227 Saskatchewan Drive, Edmonton, Alberta, T6G 2G2, Canada. E-mail: Usha.Hemraz@nrc-cnrc.gc.ca; hicham.fenniri@um6p.ma*

[b]*Nanotechnology Research Centre, National Research Council of Canada, 11421 Saskatchewan Drive, Edmonton, Alberta, T6G 2M9, Canada*

[c]*Human Health Therapeutics, National Research Council Canada, 6100 Royalmount Avenue, Montreal, Quebec, H4P 2R2, Canada*

[d]*University Mohammed VI Polytechnic, Lot 660, Hay Moulay Rachid, 43150 Benguerir, Morocco*

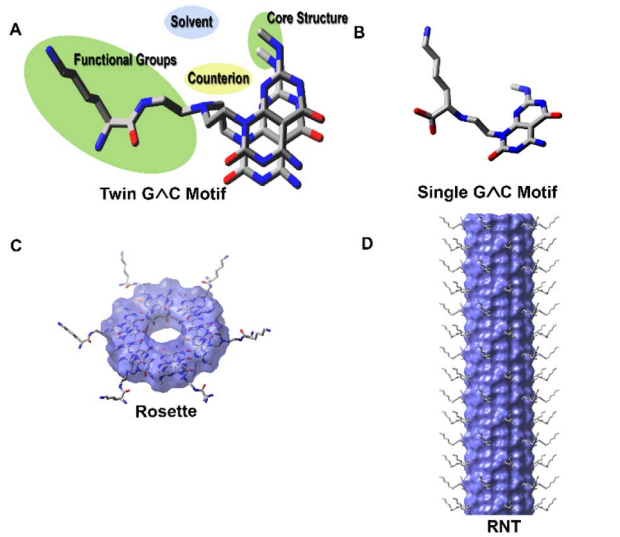

Fig. 1 Twin G∧C motif functionalized with L-lysine **1T** (A), single G∧C motif functionalized L-lysine **1S** (B), double stacked hexameric rosette formed from the association of 6 twin G∧C motifs **1T** (C) and rosette nanotube (RNT) (D).

Compared to the single G∧C system (B), the twin (A) G∧C system shown in Fig. 1 has enhanced stability due to greater preorganization and amphiphilic character, increased number of intermolecular hydrogen bonding interactions, lower charge density and steric repulsion on their outer surface.[26] These attributes are reflected in the association free energy, which is approximately twice that of the single G∧C analogue at any given length. The twin-G∧C system self-organizes into the lower energy syn conformer to produce RNTs, as shown in Fig. 1. Given the inherent advantages of having a robust twin-RNT system for several applications, we wanted to explore the variables that could optimize the self-assembly process of the twin-G∧C motif. In this report, we looked at how the twin RNT stability could be tuned with the (1) solvent system and (2) counterions as well as by the structural aspects of the motif itself including the (3) attached functional groups and (4) core structure, to bring about subtle changes in self-assembly. We also designed some single G∧C analogues and investigated how the net charge and the functional group density can inhibit self-assembly, and used hydrogen bond donor/acceptor properties of the solvents to trigger the formation of RNTs.

Results and discussion

Thirteen twin-G∧C motifs were synthesized as presented in Table 1 that were both unfunctionalized (**2T**) and functionalized with primary amines (**3T–5T**), alcohols (**6T**) aliphatic (**7T–10T**, **12T**), L-lysine (**1T**, **11T**) and aromatic groups (**13T**). A selected number of single G∧C building blocks (**1S**, **4S**, **6S**, **8S**, **11S**) were also synthesized. The general synthetic strategy involved a reductive amination reaction of an aldehyde precursor with the R^1 functional group (Scheme S1). The protected single G∧C modules were subjected to a second round of reductive amination to produce the protected twin-G∧C compounds. The resulting molecules were deprotected under acidic conditions using trifluoroacetic acid (TFA) in thioanisole to produce the single and twin-G∧C building blocks as TFA salts or HCl salts, after treatment with hydrochloric acid. The structure and purity of all new molecules were established using ^{1}H and ^{13}C NMR, HR-MS and elemental analysis (see SI). The synthesis of motifs **1S**,[26] **1T**,[26] **4T**,[30] **9T**,[27] **10T** (ref. 27) and **11T** (ref. 27) have previously been reported.

Solvent and counterions

As with all self-assembled systems, the surrounding environment is crucial for the formation and stability of RNTs and appropriate adjustments can be used to fine-tune the properties of these materials. In previously reported studies of **1T**, the self-assembly was performed under pH conditions which correlated to the protonation sites of the L-lysine side chain.[26] Three different aggregation states corresponding to short well-dispersed RNTs, ribbons and superhelicies were observed under acidic (pH 4), neutral (pH 7) and basic (pH 11) conditions, respectively. Temperature dependent circular dichroism (CD) studies of **1T** also showed that the RNTs are very stable and can persist at 95 °C.[26] At higher temperatures, the RNT aggregates dissociate back to their monomers and upon cooling, reassociate into RNTs once again.[26] Along with the pH and temperature, the surrounding media is equally important to the self-assembly and stability of the RNTs. While these supramolecular structures can be formed in both polar and non-polar solvents, for biomaterials applications, we have focused on their assembly under aqueous conditions. In this solvent environment, the aggregation is an entropically driven process,[39,40] whereby water molecules are released into the bulk solvent as rosettes are sequestered onto the growing RNTs.

As a means of optimizing the twin-RNT formation in this polar media, the self-assembly of the model compound **4T** with a butyl ammonium pendant and isolated as the TFA salt, was studied in neat and binary mixtures of MeOH (0%, 25%, 50%, 75%, 95% 99%) (Fig. 2A–F) in water. The graph in Fig. 2G depicts the percentage growth in total RNT length (with respect to the 99% MeOH solution F) that is measured in each of the scanning electron microscopy (SEM) images (Fig. 2A–F) after 1 day of aging in the respective solvent mixtures. Although rosette formation is a spontaneous and quantitative process, the RNTs that are quantified in each image and by dynamic light scattering (DLS) (Fig. 2H), are only those which have π–π stacked into RNTs of detectable length. In this approach, it was assumed that the RNT distributions on the grid were randomized and that after the self-assembly process was complete, all solutions would have the same net assembly irrespective of the solvent ratio. A nearly linear increase in percent growth in RNT length with higher concentrations of MeOH was observed (Fig. 2G). Clearly, MeOH is more favourable for RNT stability because of the decreased solvation of the donor and acceptor sites on the G∧C monomers. The integrity of the hexameric rosettes within the RNTs are better maintained by the stronger H-bonding interactions. In addition to more abundant RNT density, the solvent system also affects the length distribution of

Table 1 Functionalized twin-G∧C motifs **1T–13T** and single G∧C modules (**1S**, **4S**, **6S**, **8S**, **11S**). With the exception of **12T** where R^2 is a methyl group (Me), all other building blocks have R^2 as a hydrogen atom

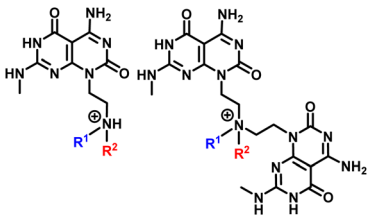

N	R^1	R^2	Single G∧C motif (S)	Twin G∧C motif (T)
1	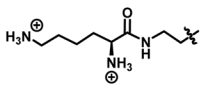	H	**1S**	**1T**
2	H	H	—	**2T**
3		H	—	**3T**
4	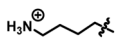	H	**4S**	**4T**
5	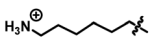	H	—	**5T**
6	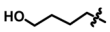	H	**6S**	**6T**
7		H	—	**7T**
8		H	**8S**	**8T**
9		H	—	**9T**
10		H	—	**10T**
11	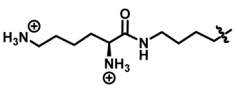	H	**11S**	**11T**
12		Me	—	**12T**
13	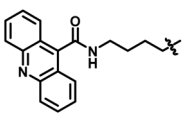	H	—	**13T**

the RNTs. The RNT's length was categorized into three groups: 10–100 nm (short tubes), 101–300 nm (medium sized tubes) and 301–2000 nm (long tubes) (Fig. S1), where the RNT length distribution is shown in the histograms for model compound **4T**. About 90% of RNTs consist of short to medium-sized nanotubes that are less than 300 nm for the 0–75% MeOH solution samples (A–D). In contrast, about 40% and 80% of the total visible RNTs range between 300-2000 nm for E and F, which have a 95% and 99% MeOH ratio, respectively. UV-vis spectroscopy was also used to monitor self-assembly of **4T** over time (Fig. 2K). Further insight into the growth of RNTs **4T** in neat MeOH was obtained using DLS. As shown in Fig. 2H, there was an increase in the apparent hydrodynamic diameter over time, which was expected as the RNTs grow in length. Upon closer inspection, a sigmoidal curve (from the inset, I) within the first few hours, identified the autocatalytic nature of the RNTs, in which a larger number of seed aggregates shown in Fig. 2J template longer RNTs and bundles in the solution as the sample ages. UV-vis spectroscopy has been used extensively for investigating nucleic acid structure and stability. It is often predicted that a hyperchromic effect is equivalent to the melting of DNA, however Williams and coworkers[41] reported that in some cases UV-vis spectroscopy fails to be an adequate technique in correlating the hyperchromic effect to disassembly. In our case, the 4T RNTs absorb UV light between 220-320 nm due to chromophores present in the G∧C base. A significant hyperchromic effect (0.5 h → 10 d) and a small hypsochromic effect (λ_{max} = 234 nm, 0.5 h → λ_{max} = 229 nm, 10 d) were observed. We believe that RNTs formation in methanol starts immediately after dissolution (as observed by SEM), so the UV absorbance might just be associated with the formation of RNTs. Over time, RNTs concentration and length increased, and this may be correlated to the hyperchromic effect observed. This is also consistent with increased scattering

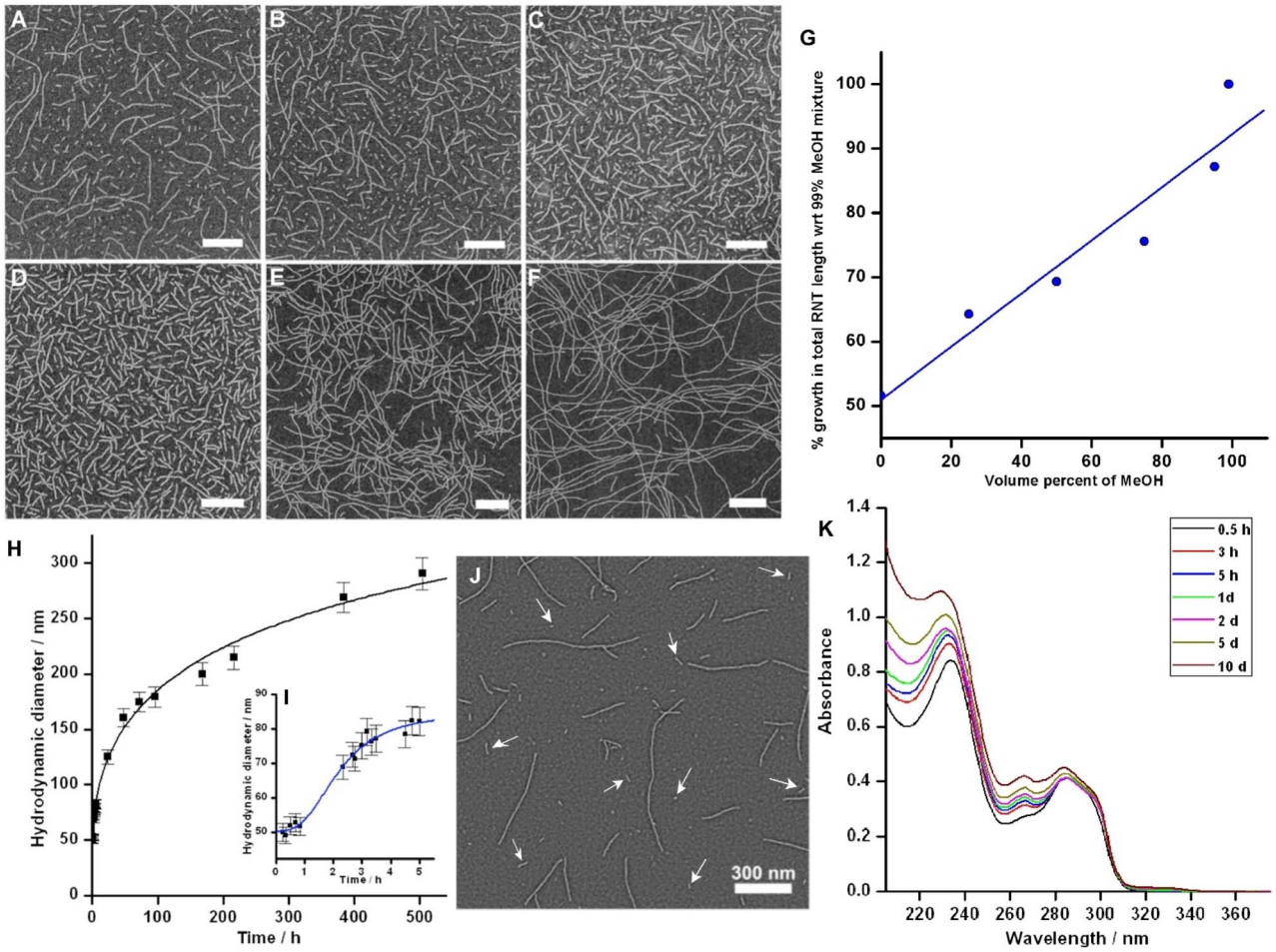

Fig. 2 SEM images of **4T** in MeOH–water mixtures: 100% water (A), 25% MeOH (B), 50% MeOH (C), 75% MeOH (D), 95% MeOH (E), 99% MeOH (F). Scale bar = 200 nm. Graph of percentage growth of RNTs with respect to 99% MeOH solution as a function of solvent mixture shown in (A)–(F) and (G). DLS spectrum of **4T** in neat MeOH (H), showing autocatalytic nature of RNT synthesis (I). SEM image of RNTs **3** in neat MeOH after 30 min of aging, highlighting the seed aggregate (J). UV-vis spectroscopy of **4T** in neat MeOH, monitored over time (K).

observed as the particles grow from shorter to longer tubes, as observed by DLS and SEM.

Solvent properties can modulate the RNT stability, size distribution and supramolecular chirality of RNTs. We have previously shown that a motif bearing a single G∧C base functionalized with L-lysine, self-assembled in water and MeOH to give RNTs with opposite chiralities, and computation revealed that the solvent molecules located in the pockets of the RNT surface act as a molecular switch in determining the RNT chirality.[42] To establish whether a similar effect would be observed with the chiral twin-G∧C motifs **1T**, **9T**, **10T** and **11T** as the TFA salts, their self-assembly was performed MeOH and water and monitored by CD spectroscopy. The nature of the solvent only affected the twin G∧C RNTs **11T** and a supramolecular switch, triggered by an achiral solvent, was observed.[27] In this study, we aimed to explore the influence of residual water, constituting less than 1%, on the self-assembly behavior of RNTs in a methanolic solution. Four twin monomers (**3T**, **4T**, **10T**, and **11T** as HCl salts) were prepared in 99.8% HPLC-grade methanol and allowed them to age for one day, followed by the addition of dried molecular sieves to eliminate residual water. The SEM images revealed that initially long and well-dispersed RNTs transformed into thick bundles (Fig. S2). These observations led us to conclude that trace amounts of water are vital for the self-assembly and dispersibility of RNTs, as their removal resulted in aggregation and precipitation. We propose that trace water molecules in the methanol solution provide the initial solvation layer in pockets and around the RNT surface. The nanotubes are preferentially solvated by water because it is a superior solvent for ions compared to methanol. Removing this hydrophilic solvation shell results in less charged RNTs due to the formation of tighter ion pairs in methanol. Consequently, dispersion decreases as water content diminishes, leading to thicker bundles. As water molecules are absorbed by the drying agent, larger aggregates form, eventually precipitating out of solution. In addition to solvent selection, further enhancement of the stability of twin-motif RNTs can be achieved by choosing appropriate G∧C base counterions. As illustrated in Fig. 3, RNTs from building blocks **1T**, **9T**, **10T** and **11T** with TFA counterions in methanol (A–D), are notably shorter compared to those with

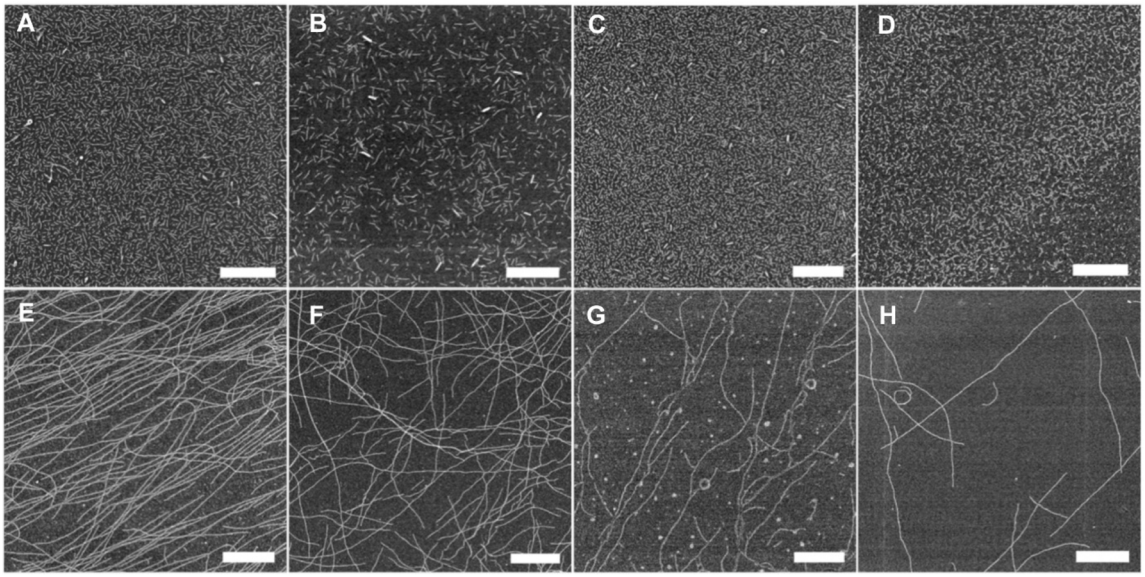

Fig. 3 SEM images of twin G∧C building blocks **1T**, **9T**, **10T** and **11T** as the TFA salts (A–D) and HCl salts (E–H) respectively, in MeOH after 1 day of aging. Scale bar = 300 nm.

Cl^- counterions (E–H). For self-assembled systems, the association free energy, an indicator of RNT stability, depends on both the association internal energy and association solvation free energy. Assuming that the molecular geometry of an RNT remains consistent regardless of solvent, the variation in association free energies between different counterions should solely reflect differences in association solvation free energy. The association solvation free energies, defined as the sum of solvation entropy and solvation energy (excluding enthalpy due to isochoric conditions), are nearly identical for both Cl^- and TFA ions. Modeling calculations have revealed that in methanolic solutions, the strongly solvated Cl^- ions enhance the association solvation free energy more effectively than the less solvated TFA ions.[43] This could be applicable to the twin RNT system as well, with a higher overall association free energy for the RNT-Cl^- system, leading to more stable RNTs of a given length in methanol, as observed in the SEM images (Fig. 3). Conversely, in water, the counterions had no effects and the effect on self-assembly was indistinguishable by SEM imaging on RNTs **9T** and **10T** (Fig. S3). It is speculated that in water any increase in solvation energy (which opposes RNT formation) gained with Cl^- ions was counterbalanced by a decrease in solvation entropy (favoring RNT formation).

Functional groups

In addition to the environmental factors, the properties of the functional groups covalently attached to the hydrophobic G∧C core are perhaps most crucial to the self-assembly and stability of the RNTs. Since these groups are expressed on the periphery of the nanotubes, their hydrophobicity and charge density strongly influence the self-assembly process, particularly in highly polar solvents such as water and MeOH. This was demonstrated by comparing the self-assembly through SEM imaging of twin-RNTs having functional groups with the same alkyl chain length of 4 atoms, but have either charged (**4T**, NH_3^+), polar (**6T**, OH) or neutral (**8T**, Me) at the terminal ends. The more hydrophobic building block **8T** have more than 53% of the RNTs were greater than 300 nm in length, whereas for **3** and **5** this corresponded to only 37% and 16% of the RNT population (Fig. S4). We believe that the hydrophobic effect of the non-polar alkyl chain on **8T** contributes to the enhanced association and growth of the longer RNTs in the aqueous solvent, while the charged and polar side-chains of **4T** and **6T** stabilize the rosettes, thereby inhibiting the growth of longer tubes. A further example demonstrating the importance of the hydrophobic effect are RNTs **7T** and **8T** (Fig. 4 and S4), where both display non-polar R^1 alkyl groups (Me and pentyl respectively) but the presence of a longer alkyl chains has more abundant and longer nanotubes. Subtle changes in the charge density of the functional groups such as the sequential addition of a methylene group also have significant effect on the self-assembly process, as illustrated with **2T–5T** (Fig. 4A–D and S5). While the population of RNTs below 200 nm increased dramatically in MeOH from 22% to 93% from **2T–5T**, RNTs greater than 300 nm in length decreased substantially. This could presumably be due to the increased steric stability from a longer side chain and as the charge separation between the protonated amine at the branch point between the two G∧C bases and the terminal ammonium ion. While studies up to this point focused on twin-motifs that featured one functional group, bis-alkylated adducts such as **12T** which is dimethylated is an interesting candidate since the charge density (+1) on the alkylated nitrogen atom is independent of pH. With a theoretical interplanar separation between the rosettes of around 4.0 Å,[26,44] this pocket should be able to accommodate functional groups with a diameter less than 4.0 Å if the π–π stacking interactions are to be maintained. Keeping in mind that the

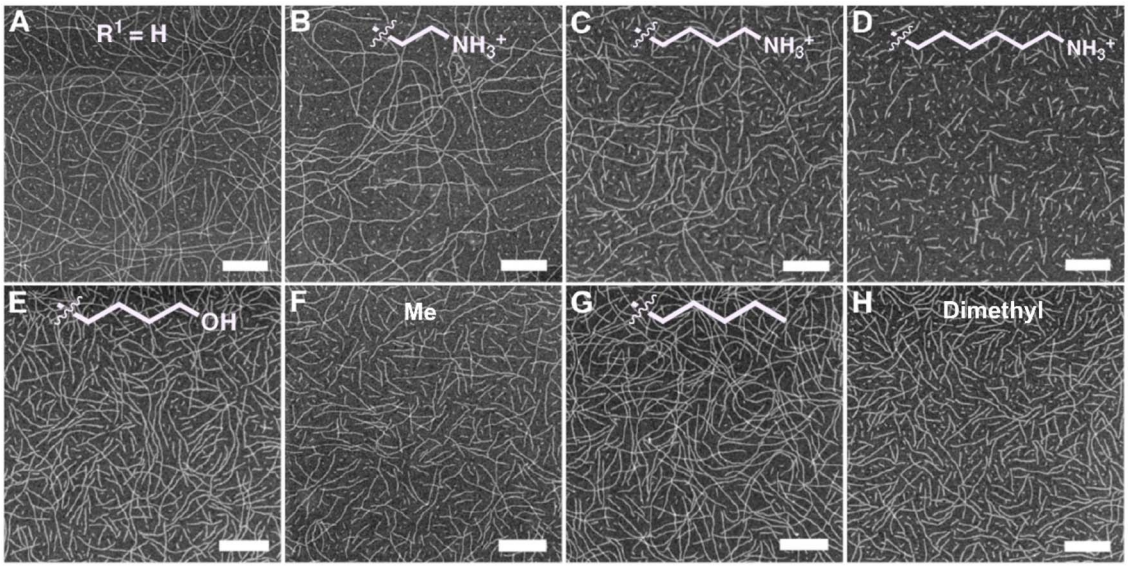

Fig. 4 SEM images of **1T–7T** (A–G), **12T** (H) in water, aged for 1 day. Scale bar 200 nm.

charge of the functional group will also impact the distance, angle and arrangement (*syn vs. anti*) of the two G∧C bases within a twin-motif, which in turn will alter the stability of the RNTs. The SEM images of RNTs **12T** (Fig. 4H) were very similar in length compared to **7T** (Fig. 4F) which has only one methyl group but has the same charge density in the protonated state. Similar RNT stability was expected since the diameter of this neutral methyl group is within the 4.0 Å limit.[45]

To further the scope of the twin-motif functional group studies, the twin-G∧C motif coupled to acridine was synthesized. Several aromatic molecules such as acridines are significant for their antimicrobial and anticancer properties.[46–50] More pertinent to these studies however, is their known ability to intercalate nucleic acids[51–54] and exhibit several polymorphic structures in the solid state due to strong electrostatic and π–π interactions.[55–57] The self-assembly of **13T** into RNTs would demonstrate the selectivity and stability of these architectures in the presence of molecules which could alter the self-assembly pathway and supramolecular structure formed. Long and well-dispersed RNTs were observed in both MeOH and water, thereby confirming the robust nature of the twin-RNTs (Fig. S6). As the stock solutions were aged over longer time periods, thicker bundles emerged (Fig. 5). Transmission electron microscopy (TEM) images (Fig. S7) of **13** established that the outer diameter of the RNTs was 5.2 nm which is in agreement with the theoretical value of 5.1 nm, whereby the acridine units are extended out from the periphery of the RNT (Fig. S8 and S9). Although this measurement suggests the acridine molecules were not intercalating the G∧C motifs within its own RNT, their intercalation with neighbouring RNTs as the bundles form over time could not be ruled out. Thus, the self-assembly was monitored by UV-vis spectroscopy. As shown in Fig. 5, there were some spectral differences of **13T** when self-assembled in water or MeOH due to solvent polarity.[58–60] Both acridine and the nucleobase residues exhibit intense absorption bands in the UV region between 200 and 300 nm, making this range unsuitable for monitoring acridine–base interactions.[61,62] The acridine fragment also shows weaker absorption bands between 325 and 400 nanometres – a region free from G∧C residue absorptions—so this range was selected to track potential spectral changes associated with the acridine moiety. It was hypothesized that if the acridine unit were intercalated between two twin rosettes, a significant hypochromic effect would occur due to π–π stacking interactions. However, the absence of hypochromism in this region for both water and methanol samples ruled out the possibility of intercalation. This suggests that π–π stacking interactions between G∧C rosettes and acridine units of neighbouring RNTs, or between acridine units within the same RNT, did not occur during RNT growth. This interpretation is consistent with molecular modelling calculations, which indicate that the distance between acridine groups within an RNT exceeds 10 Å – a separation too large to permit effective π–π stacking interactions. The absorption bands around 250 nm are attributed to the π → π* transitions of the acridine fragment, while the bands near 240 nm originate from the G∧C moieties. A significant hypochromic effect at $\lambda_{max} = 250$ nm was observed, consistent with π–π stacking interactions among double-stacked hexameric rosettes, reflecting increased self-assembly over time. At the early stage of self-assembly (1 hour), a red shift was observed between 280 and 300 nm when comparing samples in water and methanol. This was attributed to methanol's lower polarity and weaker hydrogen bonding, which reduces the ground-state stabilization and shift the π → π* transition to longer wavelengths.

Modifications to the core structure

The twin G∧C motif self-organizes into a lower energy syn conformer shown in Fig. 1A, whereby the CH_3NH groups are positioned on the same side. This preorganization is essential in forming the initial hexameric rosettes that are then further organized into the RNTs. While the relatively small methyl

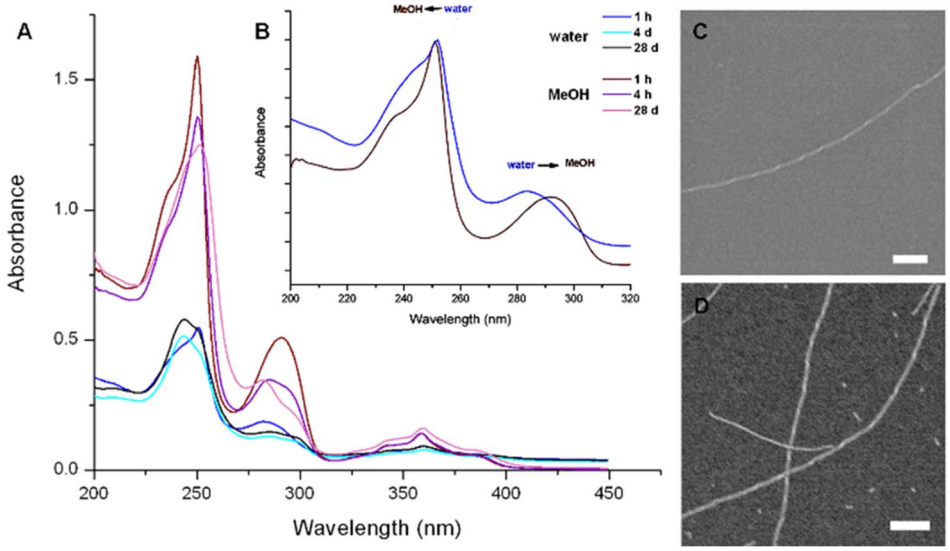

Fig. 5 UV-vis spectra of **13T** in MeOH and water (A). Inset after 1 hour of self-assembly highlighting the blue shift and red-shift in going from water to MeOH (B). SEM image of **13T** showing helical RNTs in water after 14 days of aging (C), in MeOH after 3 days of aging (D). Scale bar 200 nm.

group on this exocyclic nitrogen does not sterically inhibit the stacking of these rosettes, bulkier substituents could impart destabilization on the RNT. To test this theory, analogues of **4T** with hydrogen, ethyl and methyl as R_1 and R_2 group were synthesized and self-assembled in MeOH (Fig. 6 and S10). Although TEM measurements revealed that the diameters of **4T** (with a methyl group on the exocyclic nitrogen of each G∧C (A), **4T-H** (with a hydrogen atom on the exocyclic nitrogen on each G∧C) (B) **4T-E** (with an ethyl group on the exocyclic nitrogen on each G∧C) (C) and **4T-M** (with a hydrogen atom on the exocyclic nitrogen of one G∧C and a methyl group on the exocyclic nitrogen of the second G∧C) were of negligible difference, the lengths of RNTs **4T-E** were shorter (234 ± 92 nm) than the other three, which spanned in the micrometre range (Table S1). This demonstrates that functional groups on the exocyclic nitrogen larger than methyl do in fact destabilize the RNTs as the rosettes π–π stack and thereby provides yet another alternative means of tailoring the stability of the RNTs. Given that the self-assembly of RNTs is a dynamic and reversible process, a large standard deviation in the length of the RNTs was expected and observed. The values obtained from AFM (2.9 ± 0.2, 3.0 ± 0.1, 3.0 ± 0.2 and 3.0 ± 0.1 nm for **4T**, **4T-H**, **4T-E** and **4T-M**, respectively) were lower than those obtained by TEM (3.5 ± 0.2, 3.5 ± 0.2, 3.6 ± 0.2, 3.6 ± 0.2 for **4T**, **4T-H**, **4T-E** and **4T-M**, respectively) due to compression arising from the interaction with the tip (Table S1). RNTs are soft materials and when AFM measurements are carried out, sample deformation from substrate compression and interactions with the AFM tip can lead to flattening of the tubes, resulting in an inferior value.[63]

Self-assembly for single G∧C systems

The existence of built-in features in the chemical structure of a building block does not always guarantee the formation of RNTs. While the twin RNTs has enhanced stability due to pre-organization, increased amphiphilic character, greater number of hydrogen bonds per module, less steric congestion and lower electrostatic repulsion, some single G∧C motifs have been shown to self-assemble.[24–26] The creation of supramolecular structures from the interaction of two or more neutral or charged species has been primarily observed in aqueous medium, however other solvents are also known to have a great impact on the stability of such superstructures.[64–68] The function of such solvent systems is not just limited to the dissolution of the solute in the medium, but also contribute immensely to the existence and stability of such architectures by favourable solute–solvent interactions. A head-to-head comparison between modules **1S** and **1T** showed that unlike the latter, the former did not form any RNTs in aqueous or methanolic conditions. It was hypothesized the existence of intramolecular hydrogen bonding could block the cytosine face of the G∧C base from engaging in intermolecular hydrogen bonding, preventing self-assembly. We could also not discount the environmental factors that could influence the stability and self-assembly of the RNTs. As such, the self-assembly was investigated in different solvent systems (Table 2). For most derivatives (with the exception of **8S**), no self-assembly was observed upon dissolution in water (Fig. S11). Since the monomers were isolated as either HCl or TFA salts, the pH of the resulting aqueous solutions was about 4, and under these conditions, the nitrogen atoms on the side-chain of the monomers exist in the protonated form, leading to high charge repulsion, which hinders RNT formation. A trend was observed between the net charge on the monomers and their ability to self-assemble. Although **6S** had similar net charge as **8S**, no nanostructures were observed in solution. This could be related to the stability and solvation of the monomer, resulting from the hydrophilicity of the terminal hydroxyl group in the medium. In water, aggregation is driven

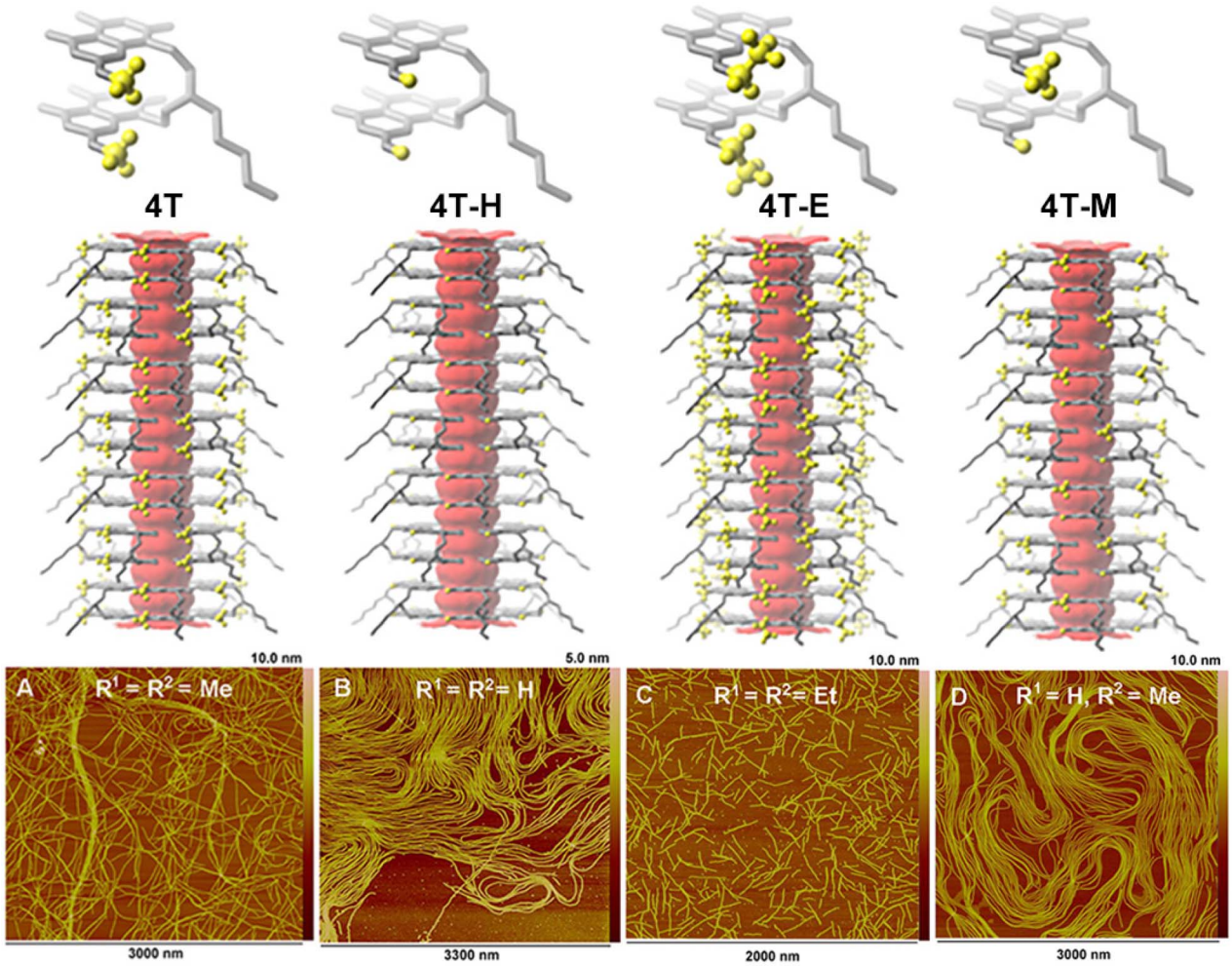

Fig. 6 Atomic force microscopy (AFM) image of **4T**, **4T-H**, **4T-E** and **4T-M** (A–D) in MeOH respectively after 1 day of aging (A). The outer diameter of (A–D) from the AFM images was determined to be 2.9 ± 0.2, 3.0 ± 0.1, 3.0 ± 0.2 and 3.0 ± 0.1 nm, respectively.

Table 2 Self-assembly of single G∧C motifs in different solvents

Single G∧C			**1S**	**4S**	**6S**	**8S**	**11S**
Net charge			+3	+2	+1	+1	+3
Solvent	Solvent type	Dielectric constant	Self-assembly				
Water (pH 4)	HBA/HBD	78	✗	✗	✗	✓	✗
Water (pH 11)	HBA/HBD		✗	✗	✓	✓	✗
Methanol	HBA/HBD	33	✗	✗	✓	✗	✗
DMF	HBA	38	✓	✓			✓
DMA	HBA	38	✓	✓			✓
DMSO	HBA	47	✗	✗			✗

by entropy and water molecules are released into the bulk solvent as rosettes are sequestered onto the growing RNTs. In addition, the hydrophobic nature of the side-chain in **8S** contribute to the self-assembly.[9–11] Evidence that the net charge plays a significant role in the self-assembly of these monomers was demonstrated by successful RNT formation in the case of **6S**

at pH 11, where the nitrogen atoms would be unprotonated, reducing electrostatic repulsion (Fig. S12). These conditions were still not favourable for the self-assembly of **1S**, **4S** and **11S**, and other solvents were therefore explored. In methanol, there are stronger electrostatic interactions between the ammonium groups on the G∧C base and the chloride anions than in water due to decreased cation and anion solvation.[43,69,70] The charge neutralization resulting from the tighter ion pair, reduces the charge density on the RNTs, justifying the presence of nanostructures for **6S** in methanol and its non-assembly in water (Fig. S13). So far, only the molecules with the lowest charge density showed higher order aggregation and the monomers **1S** and **11S** have higher functional group densities, could not. Water and methanol are amphiprotic solvents, which can act both as a hydrogen-bond donor (HBD) and hydrogen-bond acceptor (HBA).[70] We envisaged that the high positive charge density on the RNTs would be better stabilized in a HBA solvent. We thus investigated dimethyl sulfoxide (DMSO) and *N*,*N*-dimethylformamide (DMF) and *N*,*N*-dimethylacetamide (DMA) as solvents for the self-assembly of compounds (Table 2, Fig. S14 and S15). DMF is a dipolar aprotic solvent and possesses both donor and acceptor properties. However the absence of a strong proton-donor group limits the extent of H-bonding due to which liquid DMF does not form chains or lattices. As such, DMF can be considered as a HBA solvent. One of the most striking differences in the physical properties of water and DMF is the dielectric constant. The higher the dielectric constant, existence of ion pairs would be less prevalent due to the greater charge separation. In addition, the partial molar volume of ions determines the type and the strength of the ion-pair in solution. In water, the chloride ion displays a partial molar volume of 24.3 $cm^3\ mol^{-1}$, whereas in DMF the partial molar volume is 2.8 $cm^3\ mol^{-1}$. While the change in partial molar volume of the chloride ion from water to DMF is quite alarming, the difference in partial molar volume of the cations is relatively small. For instance, the difference in partial molar volume of tetramethylammonium ions is only 1.1.[71] The lower solvation in DMF and DMA leads to a tighter ion pair between the ammonium and chloride ions, thus leading to more stable RNTs due to less electrostatic repulsion. Unlike the DMF and DMA samples, the DMSO samples failed to display any nanostructures. Although, we do not have a definite answer to the non-assembly under these conditions, we presume that it could be related to the polarity of the solvent. Compared to DMF and DMA, DMSO has a higher dipole moment, which can lead to more interference with the H-bonding pattern within the rosettes and the stacking of the RNTs. 2D NMR experiments were carried out to investigate any intramolecular hydrogen bonding within the monomers that could hinder the self-assembly. The absence of through space correlation from the TROESY spectra negates this hypothesis (Fig. S16–S19).

Conclusion

The self-assembly and stability of twin-RNTs are dictated by a delicate yet highly tuneable balance between solvent environment and molecular architecture. Solvent selection emerges as a decisive factor, influencing both the solvation of the G∧C motif and the behaviour of associated counterions. In methanol, reduced solvation of donor and acceptor sites enhances hydrogen bonding within the hexameric rosettes, resulting in greater structural integrity, while counterions such as chloride, with their favourable solvation free energy, further stabilize the nanotube assemblies. The design and intrinsic structural features of the twin-G∧C motif are the primary determinants of supramolecular stability, highlighting the critical influence of molecular architecture on RNT behaviour. In polar solvents, hydrophobic and electrostatic effects can be harnessed to promote the formation of longer, more stable nanotubes. However, steric interference from bulky adducts or substitution of a methylamine with an ethylamine group in the core modification disrupts π–π stacking and weakens overall stability. Collectively, these findings highlight a powerful design principle: by strategically tailoring both molecular structure and solvent environment, it is possible to exert fine control over RNT stability and morphology. This insight not only deepens our understanding of supramolecular assembly but also opens new avenues for engineering functional nanomaterials with programmable properties.

Author contributions

The manuscript was written through contributions from all co-authors. All authors have given approval to the final version of the manuscript.

Conflicts of interest

The authors declare no competing financial interest.

Data availability

The experimental section and data supporting this article has been included as part of the supplementary information (SI). Supplementary information: synthetic procedures, self-assembly, microscopy characterization, molecular modeling, DLS data and NMR spectra. See DOI: https://doi.org/10.1039/d6na00217j.

Acknowledgements

This work was funded by the National Research Council of Canada, a Federal Research and Development Organization of the Government of Canada and the University of Alberta.

References

1 A. Klug, *Angew. Chem., Int. Ed. Engl.*, 1983, **22**, 565–582.
2 N. C. Seeman, *Angew. Chem., Int. Ed. Engl.*, 1998, **37**, 3220–3238.
3 Y. Zhao, S. Song, X. Ren, J. Zhang, Q. Lin and Y. Zhao, *Chem. Rev.*, 2022, **122**, 5604–5640.
4 C. Piguet, G. Bernardinelli and G. Hopfgartner, *Chem. Rev.*, 1997, **97**, 2005–2062.

5 J. M. Lehn, A. Rigault, J. Siegel, J. Harrowfield, B. Chevrier and D. Moras, *Proc. Natl. Acad. Sci. U. S. A.*, 1987, **84**, 2565–2569.
6 D. Zhao, T. van Leeuwen, J. Cheng and B. L. Feringa, *Nat. Chem.*, 2017, **9**, 250–256.
7 K. Ariga, T. Mori, T. Kitao and T. Uemura, *Adv. Mater.*, 2020, **32**, e1905657.
8 T. L. Schlick, Z. Ding, E. W. Kovacs and M. B. Francis, *J. Am. Chem. Soc.*, 2005, **127**, 3718–3723.
9 B. Widom, P. Bhimalapuram and K. Koga, *Phys. Chem. Chem. Phys.*, 2003, **5**, 3085–3093.
10 N. T. Southall, K. A. Dill and A. D. J. Haymet, *J. Phys. Chem. B*, 2002, **106**, 521–533.
11 L. R. Pratt and A. Pohorille, *Chem. Rev.*, 2002, **102**, 2671–2692.
12 C. A. Hunter, K. R. Lawson, J. Perkins and C. J. Urch, *J. Chem. Soc., Perkin Trans. 2*, 2001, 651–669.
13 J. Rebek Jr, *Angew. Chem., Int. Ed.*, 2005, **44**, 2068–2078.
14 C. Schmuck, *Angew. Chem., Int. Ed.*, 2007, **46**, 5830–5833.
15 C. Gaeta, P. La Manna, M. De Rosa, A. Soriente, C. Talotta and P. Neri, *ChemCatChem*, 2021, **13**, 1638–1658.
16 V. Lopez-Corbalan, A. Fuertes, A. L. Llamas-Saiz, M. Amorin and J. R. Granja, *Nat. Commun.*, 2024, **15**, 6055.
17 A. M. Carmona-Ribeiro, *Chem. Soc. Rev.*, 2001, **30**, 241–247.
18 W. Cui, J. Li and G. Decher, *Adv. Mater.*, 2016, **28**, 1302–1311.
19 M. Dymek and E. Sikora, *Adv. Colloid Interface Sci.*, 2022, **309**, 102757.
20 C. F. van Nostrum, *Adv. Mater.*, 1996, **8**, 1027–1030.
21 A. P. H. J. Schenning and E. W. Meijer, *Chem. Commun.*, 2005, 3245–3258.
22 D. Yang, M. J. Campolongo, T. N. Nhi Tran, R. C. H. Ruiz, J. S. Kahn and D. Luo, *Wiley Interdiscip. Rev.:Nanomed. Nanobiotechnol.*, 2010, **2**, 648–669.
23 K. Ariga, M. Nishikawa, T. Mori, J. Takeya, L. K. Shrestha and J. P. Hill, *Sci. Technol. Adv. Mater.*, 2019, **20**, 51–95.
24 H. Fenniri, P. Mathivanan, K. L. Vidale, D. M. Sherman, K. Hallenga, K. V. Wood and J. G. Stowell, *J. Am. Chem. Soc.*, 2001, **123**, 3854–3855.
25 H. Fenniri, B. L. Deng and A. E. Ribbe, *J. Am. Chem. Soc.*, 2002, **124**, 11064–11072.
26 J. G. Moralez, J. Raez, T. Yamazaki, R. K. Motkuri, A. Kovalenko and H. Fenniri, *J. Am. Chem. Soc.*, 2005, **127**, 8307–8309.
27 U. D. Hemraz, M. El-Bakkari, T. Yamazaki, J. Y. Cho, R. L. Beingessner and H. Fenniri, *Nanoscale*, 2014, **6**, 9421–9427.
28 C. Ai Lin, G. M. Jesus, F. Hicham and J. W. Thomas, *Nanotechnology*, 2004, **15**, S234.
29 L. Zhang, F. Rakotondradany, A. J. Myles, H. Fenniri and T. J. Webster, *Biomaterials*, 2009, **30**, 1309–1320.
30 L. Zhang, U. D. Hemraz, H. Fenniri and T. J. Webster, *J. Biomed. Mater. Res., Part A*, 2010, **95**, 550–563.
31 L. Sun, D. Li, U. D. Hemraz, H. Fenniri and T. J. Webster, *J. Biomed. Mater. Res., Part A*, 2014, **102**, 3446–3451.
32 L. Sun, L. Zhang, U. D. Hemraz, H. Fenniri and T. J. Webster, *Tissue Eng., Part A*, 2012, **18**, 1741–1750.
33 A. Childs, U. D. Hemraz, N. J. Castro, H. Fenniri and L. G. Zhang, *Biomed. Mater.*, 2013, **8**, 065003.
34 J. Y. Cho, P. Bhowmik, P. L. Polowick, S. G. Dodard, M. El-Bakkari, G. Nowak, H. Fenniri and U. D. Hemraz, *ACS Omega*, 2020, **5**, 24422–24433.
35 X. Zhou, S. Tenaglio, T. Esworthy, S. Y. Hann, H. Cui, T. J. Webster, H. Fenniri and L. G. Zhang, *ACS Appl. Mater. Interfaces*, 2020, **12**, 33219–33228.
36 P. Tripathi, L. Shuai, H. Joshi, H. Yamazaki, W. H. Fowle, A. Aksimentiev, H. Fenniri and M. Wanunu, *J. Am. Chem. Soc.*, 2020, **142**, 1680–1685.
37 U. Ho, M. El-Bakkari, A. Alshamsan, J. Y. Cho, T. Yamazaki, U. D. Hemraz and H. Fenniri, *Biomater. Sci.*, 2023, **11**, 7169–7178.
38 U. D. Hemraz, T. Yamazaki, M. El-Bakkari, J. Y. Cho and H. Fenniri, *Nanoscale Adv.*, 2024, **7**, 281–287.
39 D. Gorl and F. Wurthner, *Angew. Chem., Int. Ed.*, 2016, **55**, 12094–12098.
40 P. Dey, P. Rajdev, P. Pramanik, R. Haag and S. Ghosh, *Macromolecules*, 2020, **53**, 7044–7052.
41 T. M. Davis, L. McFail-Isom, E. Keane and L. D. Williams, *Biochemistry*, 1998, **37**, 6975–6978.
42 R. S. Johnson, T. Yamazaki, A. Kovalenko and H. Fenniri, *J. Am. Chem. Soc.*, 2007, **129**, 5735–5743.
43 C. P. Kelly, C. J. Cramer and D. G. Truhlar, *J. Phys. Chem. B*, 2006, **110**, 16066–16081.
44 D. N. Chin, E. E. Simanek, X. Li, M. I. M. Wazeer and G. M. Whitesides, *J. Org. Chem.*, 1997, **62**, 1891–1895.
45 E. A. Müller, L. F. Rull, L. F. Vega and K. E. Gubbins, *J. Phys. Chem.*, 1996, **100**, 1189–1196.
46 P. Belmont, J. Bosson, T. Godet and M. Tiano, *Anticancer Agents Med. Chem.*, 2007, **7**, 139–169.
47 T. N. Wells, P. L. Alonso and W. E. Gutteridge, *Nat. Rev. Drug Discovery*, 2009, **8**, 879–891.
48 G. Cholewinski, K. Dzierzbicka and A. M. Kolodziejczyk, *Pharmacol. Rep.*, 2011, **63**, 305–336.
49 B. Zhang, X. Li, B. Li, C. Gao and Y. Jiang, *Expert Opin. Ther. Pat.*, 2014, **24**, 647–664.
50 J. An, M. Minie, T. Sasaki, J. J. Woodward and K. B. Elkon, *Annu. Rev. Med.*, 2017, **68**, 317–330.
51 L. S. Lerman, *J. Mol. Biol.*, 1961, **3**, 18–30.
52 N. J. Pritchard, A. Blake and A. R. Peacocke, *Nature*, 1966, **212**, 1360–1361.
53 W. A. Denny, *Curr. Med. Chem.*, 2002, **9**, 1655–1665.
54 J. Franco Pinto, A. Fillion, P. Duchambon, S. Bombard and A. Granzhan, *Eur. J. Med. Chem.*, 2022, **227**, 113909.
55 R. D. Lowde, D. C. Phillips and R. G. Wood, *Acta Crystallogr.*, 1953, **6**, 553–556.
56 D. Musumeci, C. A. Hunter and J. F. McCabe, *Cryst. Growth Des.*, 2010, **10**, 1661–1664.
57 X. Mei and C. Wolf, *Cryst. Growth Des.*, 2004, **4**, 1099–1103.
58 A. W. Sangster and K. L. Stuart, *Chem. Rev.*, 1965, **65**, 69–130.
59 C. Reichardt, D. Che, G. Heckenkemper and G. Schäfer, *Eur. J. Org Chem.*, 2001, 2343–2361.
60 S. Spange, D. Kunzmann, R. Sens, I. Roth, A. Seifert and W. R. Thiel, *Chemistry*, 2003, **9**, 4161–4167.

61 D. Fornasiero and T. Kurucsev, *Chem. Phys. Lett.*, 1985, **117**, 176–180.
62 L. Pérez-Flores, A. J. Ruiz-Chica, J. G. Delcros, F. Sánchez-Jiménez and F. J. Ramírez, *J. Mol. Struct.*, 2005, **744**, 699–704.
63 J. A. DeRose and J. P. Revel, *Thin Solid Films*, 1998, **331**, 194–202.
64 H. Engelkamp, S. Middelbeek and R. J. Nolte, *Science*, 1999, **284**, 785–788.
65 M. Ikeda, T. Nobori, M. Schmutz and J. M. Lehn, *Chemistry*, 2005, **11**, 662–668.
66 J.-M. Lehn, *Angew. Chem., Int. Ed. Engl.*, 1990, **29**, 1304–1319.
67 A. Marsh, M. Silvestri and J.-M. Lehn, *Chem. Commun.*, 1996, 1527–1528.
68 M. Mascal, N. M. Hext, R. Warmuth, M. H. Moore and J. P. Turkenburg, *Angew. Chem., Int. Ed. Engl.*, 1996, **35**, 2204–2206.
69 I. Persson, *Pure Appl. Chem.*, 1986, **58**, 1153–1161.
70 C. Reichardt, *Solvents and Solvent Effects in Organic Chemistry*, Wiley-VCH, Weinheim/Germany, 2003, p. 2003.
71 Y. Marcus, *Chem. Rev.*, 2007, **107**, 3880–3897.